IET Journals
The Institution of Engineering and Technology

Millimeter-wave Multi-view Near-field Scattering Tomography System

ISSN 1751-8644
doi: 0000000000
www.ietdl.org

Shahed Shahir[1], Behrooz Semnani[1], Mehrbod Mohajer[1], Gholamreza Rafi[1], Jeff Orchard[2], Safieddin Safavi-Naeini[1]*

[1] *Electrical and Computer Engineering Department, University of Waterloo, Waterloo, ON, N2L 3G1 Canada*
[2] *David R. Cheriton School of Computer Science, University of Waterloo, Waterloo ON N2L3G1 Canada*
** E-mail: sshahir@uwaterloo.ca*

Abstract: In a previous paper [1], the authors accurately estimated the permittivity profile of object under test (OUT) from electric fields measured outside OUT by considering the region of interest confined within the boundary of the OUT. This paper proposes a continuous-wave multi-view near-field scattering tomography system at the millimeter-wave frequency range and reformulates the sub-space approach for reconstructing the continuous-wave tomographic images while considering the region of interest beyond the OUT boundary. The OUT reconstructed tomographic images enable one to localize the OUT boundaries. The proposed system also eliminates the need for fully systemic isolation (i.e. Anechoic chamber) or water as a background medium by reducing multipath effects substantially at millimeter wave. The system performance is evaluated by reconstructing the tomographic images of various samples, and the experimental results are presented.

1 Introduction

Electromagnetic Scattering Tomography system is an inspiring alternative to existing imaging modalities. The need for an alternative imaging system to complement the existing medical imaging modalities is undeniable in today's medical health care practice [2, 3]. The biological tissue screening and examinations are done by means of magnetic resonance, computed tomography (CT), x-ray, and ultrasound imaging modalities. Magnetic resonance images (MRIs) are good for imaging the soft tissues but not hard tissues (i.e. bones or teeth). CTs are used for imaging and diagnosis of the hard tissues in practice but not soft tissues [4]. Ultrasound cannot be used for imaging inside the hard tissues but can be used for imaging the outer surface of hard tissues [5]. Since all parts in a living biosystem are dielectric in nature [6], they can be considered as lossy dielectric and electromagnetic waves can penetrate inside the biosystem. For that reason, several electromagnetic imaging systems were developed [2, 3, 6–20] to meet the high demand for an alternative imaging modality for clinical applications.

Depending on the shape of the observation domain, the electromagnetic scattering based imaging systems are classified [21] into two main categories: planar imaging and non-planar imaging. A brief review of the existing planar electromagnetic scattering systems reported in literature are presented below.

Electromagnetic scattering systems for coherent projection imaging have been reported in [6–8, 22–24]. The electromagnetic scattering computerized tomography in [2, 9] was developed by ignoring the scattered field in calculation of the equivalent current, and using the Born's approximation and the Rytov's approximation. Since they assumed that electromagnetic fields propagate through a scatterer in a straight line, the transmitting and receiving antennas were moved around the stationary scatterer over 180°, similar to CT. This, however, is not a valid assumption for electromagnetic scattering imaging systems. Later, for faster scanning speed, electronic raster scanning of the electric fields was reported in [11, 21, 25–27]. Generally speaking, electronic raster-scanning-based tomographic systems suffer from certain drawbacks: 1) the measurement fields are disturbed by the antenna elements placed adjacent to the receiving antenna element, and 2) the receiving antenna elements cross-talk.

In [28, 29], the electromagnetic scattering tomography systems are implemented in an Anechoic chamber to control the multipath effects. Since an Anechoic chamber is not a feasible option for clinical applications, water is widely used as the background medium for electromagnetic scattering imaging systems to control the multipath effects and lower the contrast of the scatterer in [2, 6–11, 15, 21, 24, 25, 30, 31]. To gain images with higher resolution, higher frequencies are recommended; however, higher frequencies increase the electric field attenuation in water [32]. Thus, to enable higher frequency measurement, finding an alternative background medium with less attenuation is necessary.

To address the aforementioned issues and alleviate these difficulties, we present a new continuous-wave multi-view near-field scattering tomography (NFST) system operating at the millimeter-wave frequency range. The proposed system does not need to fully cover the lateral surface of an OUT and is the first non-linear imaging system implemented at millimeter wave. Conducting our experiment at the millimeter-wave frequency range enables us to reduce the multipath effects significantly. For lowering the cost, the transmitting antenna in the proposed system remains stationary throughout the measurement, and the probe moves over the measurement plane using an advanced scanner for measurements. Even though the mechanical scan is not as fast as an electronic scan, the proposed system does not suffer from the errors due to the field disturbance caused by the adjacent receiving antennas, the cross-talks among the antennas, coupling between the antennas, and/or the mismatch between the different channels in an electronic scan [10, 11, 21, 26, 27].

This paper is organized as follows: Section 2 reviews and formulates the electromagnetic inverse scattering problem based on the signal subspace approach. Section 3 describes our multi-view NFST system, and details the system's operational processes and calibrations. Section 4 presents the experimental results, and Section 5 concludes the paper.

2 Signal Subspace Approach

In this section, we review and reformulate the electromagnetic inverse scattering problem formulation based on the signal subspace approach. The values of the contrast factor distribution inside and outside OUT are non-zero and zero, respectively, if OUT is considered within a region of interest (ROI) where $OUT \subset ROI$. The OUT contrast factor distribution, κ_r, is complex and unknown, and is defined as follows provided that the free space is the background

medium,

$$\kappa_r \quad = \epsilon_r - 1 - j\frac{\sigma}{\omega\epsilon_0}, \tag{1}$$

where ϵ_r, ϵ_0, ω, and σ are the relative permittivity, the free space permittivity, the angular frequency, and conductivity, respectively. Since the location and boundary of the OUT are unknown, κ_r is estimated over ROI from the electric field measured over the observation plane, v_{obs}, outside ROI. Provided that, in ROI, the media have a homogenous magnetic permeability profile, the total electric field satisfies the complex vector wave equation:

$$\nabla \times \nabla \times \vec{E}_{scat} - \omega^2 \mu_0 \epsilon_0 \vec{E}_{scat} = \quad -j\omega\mu\vec{J}_{eq}, \tag{2}$$

where

$$\vec{J}_{eq} = j\omega\epsilon_0\kappa_r\vec{E}_{tot}, \tag{3}$$

$$\vec{E}_{tot} = \quad \vec{E}_{inc} + \vec{E}_{scat}, \tag{4}$$

and $\vec{E}_{tot}$, $\vec{E}_{scat}$, $\vec{E}_{inc}$, $\vec{J}_{eq}$, and μ_0 are the total electric field, the scattered electric field, the incident electric field, the volume equivalent current source (VECS), and the free space permeability, respectively. The scattered electric field can be obtained [33] as follows:

$$\vec{E}_{scat}(\vec{r}) = -j\omega\mu \int \left(1 + \frac{1}{k^2}\nabla\nabla\cdot\right) g(\vec{r},\vec{r}')\vec{J}_{eq}(\vec{r}')dv', \tag{5}$$

where k is the wave number ($\omega\sqrt{\mu\epsilon}$), and $g(\vec{r},\vec{r}')$ is the scalar Green's function,

$$g(\vec{r},\vec{r}') = \frac{e^{-j(k|\vec{r}-\vec{r}'|)}}{4\pi|\vec{r}-\vec{r}'|}, \tag{6}$$

and $\vec{r}$ and $\vec{r}'$ are the vectors that locate the observation point and the source point, respectively.

The scattered field generated by the VECS in a homogeneous medium for two dimensional TM_y can be obtained [33] as follows:

$$\vec{E}_{scat}(\vec{r}) = -j\omega\mu\hat{y}\int_{ROI} G_a(\vec{r},\vec{r}')J_{eq}(\vec{r}')dv', \tag{7}$$

where $G_a(\vec{r},\vec{r}') = \frac{H_0^{(2)}(k|\vec{r}-\vec{r}'|)}{4j}$, and the VECS has a single component in $\hat{y}$ direction ($\vec{J}_{eq} = J_{eq}\hat{y}$). The scattered electric field equation (7) can be discretized by dividing ROI into the q number of elements. By applying the Method of Moments (MOM), the scattered electric field equation (7) can be written for the p number of elements in v_{obs} in a matrix form:

$$\mathbf{E}_{scat} = \mathbf{G}_e\,\mathbf{J}_{eq}, \tag{8}$$

where $\mathbf{E}_{scat}$ is the $p \times 1$ single column matrix; $\mathbf{J}_{eq}$ is the $q \times 1$ total VECS single column matrix, and $\mathbf{G}_e$ is the $p \times q$ Green's function matrix wherein the m^{th} row and n^{th} column element of the electric field Green's function matrix , $G_{e\,mn}$, is:

$$G_{e\,mn} \quad = -j\omega\mu\int_{ROI^n} G_a(\vec{r_m},\vec{r}')dv'. \tag{9}$$

The successful estimation of the contrast factor profile depends on the solution to the inverse source problem, which is non-unique. To work around the ill-posedness of the inverse source problem, the $\mathbf{E}_{scat}$ and $\mathbf{J}_{eq}$ are transferred into the new subspaces and be represented as the spans of the new bases, u_i, and v_i, respectively,

$$E_{scat\,m} \quad = \quad \sum_{i=1}^{p} \alpha_i u_{i\,m}, \quad m = 1, 2, \cdots, p \tag{10}$$

$$J_{eq\,n} \quad = \quad \sum_{i=1}^{q} \beta_i v_{i\,n}, \quad n = 1, 2, \cdots, q \tag{11}$$

where $E_{scat\,m}$ is the m^{th} element of $\mathbf{E}_{scat}$; $J_{eq\,n}$ is the n^{th} element of $\mathbf{J}_{eq}$; α_i represents the i^{th} complex coefficient of the orthonormal basis of the scattered electric field; and β_i represents the i^{th} coefficient of the orthonormal basis of VECS. Equations (10) and (11) represent the orthogonal expansions of the scattered electric fields and VECS's, respectively. The variable α_i can be determined as follows:

$$\alpha_i \quad = \quad \sum_{m=1}^{p} u_{i\,m}^{\dagger} E_{scat\,m}, \quad i = 1, 2, \cdots, p \tag{12}$$

where $\dagger$ represents the Hermitian transpose; $u_{i\,m}$ is the i^{th} row element of the m^{th} column basis of the scattered fields, $\mathbf{U}$; $v_{i\,n}$ is the i^{th} row element of the n^{th} column basis of the source, $\mathbf{V}$; α_i is bounded and well behaved.

The VECS orthogonal coefficient, β_i, can be obtained thus:

$$\beta_i \quad = \quad \frac{\alpha_i}{s_i}, \quad i = 1, 2, \cdots, q, \tag{13}$$

where s_i represents the i^{th} diagonal element of $\mathbf{S}$ provided that the spatial Green's function representation, $\mathbf{G}$, is decomposed into the Green's function modal representation, $\mathbf{S}$, and two orthogonal matrices using the singular value decomposition as $\mathbf{G} = \mathbf{USV}^{\dagger}$. The β_i calculation is not as straightforward as the α_i calculation because the s_i decays faster than the corresponding α_i. The β_i stability directly depends on the s_i value. To discuss the β_i stability, we categorize the s_i range into three subregions: radiating, non-radiating, and noise by using two threshold indexes: L_{RAD} and L_{noise}. The first threshold index, L_{RAD}, separates the radiating VECS bases and the non-radiating VECS bases. The second threshold index, L_{noise}, separates the non-radiating VECS bases and the noise bases. Below the L_{RAD} threshold, in the radiating subregion, both s_i and α_i are bounded and well behaved. For that reason, we consider the radiating part of VECS when reconstructing the scatterer contrast factor. Thus, Equations (10), (11), (12), and (13) can be rewritten as follows:

$$E_{scat\,m}^{RAD} \quad = \quad \sum_{i=1}^{L_{RAD}} \alpha_i u_{i\,m} \qquad m = 1, 2, \cdots, p \tag{14}$$

$$J_{eq\,n}^{RAD} \quad = \quad \sum_{i=1}^{L_{RAD}} \beta_i v_{i\,n} \qquad n = 1, 2, \cdots, q \tag{15}$$

$$\alpha_i \quad = \quad \sum_{m=1}^{p} u_{i\,m}^{\dagger} E_{scat\,m}^{RAD} \quad i = 1, 2, \cdots, L_{RAD} \tag{16}$$

$$\beta_i \quad = \quad \frac{\alpha_i}{s_i} \qquad\qquad i = 1, 2, \cdots, L_{RAD} \tag{17}$$

If the non-radiating subregion is represented by the spans of the bases with the indexes between L_{RAD} and L_{noise}, s_i starts decaying very quickly in the non-radiating subregion. Thus, β_i rises exponentially. The larger β_is could dominate and affect the results improperly if the non-radiating VECS properties are not taken into consideration. In the noise subregion, the s_i value fluctuates around zero, with many sign changes. In the subregion, the inverse source problem is unstable.

The planar NFST system's noise level, N_{level}, is defined as follows:

$$N_{level} = \quad \begin{cases} pa_{fp}a_{sm}, & q < p, \\ qa_{fp}a_{sm}, & p \leq q, \end{cases} \tag{18}$$

where a_{fp} and a_{sm} are the CPU floating-point relative accuracy and the measurement sampling accuracy, respectively. The L_{noise} is the index of the system noise level, and L_{RAD} is the modal threshold and will be discussed below in detail. In fact, the first L_{RAD} bases represent the radiating bases; the bases between $L_{RAD}+1$ and $L_{noise}-1$ represent the non-radiating bases; and the bases beyond L_{noise} represent the noise bases of the planar NFST system. The radiating part of VECS is used to calculate the radiating part of the

contrast factor of a scatterer from the scattered fields measured at v_{obs}. The radiating VECS is proportional to the radiating contrast factor and inversely to the radiating internal total field as depicted in Equation (23) in [1]. Thus, the radiating contrast factor can be obtained by using the radiating part of VECS (15), and is defined as,

$$\kappa_{r\,n}^{RAD} = J_{eq\,n}^{RAD} / \left(j\omega\epsilon_0 E_{tot\,n}^{int\,RAD} \right), \quad n = 1, 2, \cdots, q \quad (19)$$

where $J_{eq\,n}^{RAD}$ and $E_{tot\,n}^{int\,RAD}$ are the corresponding *radiating* VECS and total electric field at a point, r_n, denoted by n. The *radiating* internal total electric field, $E_{tot\,n}^{int\,RAD}$ is now defined by

$$E_{tot}^{int\,RAD}(r_n) = E_{inc}(r_n) + E_{scat}^{int\,RAD}(r_n), \quad (20)$$

where

$$E_{scat}^{int\,RAD}(r_n) = -j\omega\mu \int_{ROI} G_a(r_n, r') J_{eq}^{RAD}(r') dv', \quad (21)$$

and $r_n \in$ ROI and $r' \in$ ROI. In contrast with the Born's approximation, which makes the above equation linear by replacing the incident field with the total electric field, Equation (19) is non-linear, as both the nominator and denominator in (19) are the function of the radiating VECS in this process.

The radiating contrast factor is estimated by extending the aperture size artificially and conducting multi-view tomography (known also as Synthetic Aperture Tomography or SAT) instead of applying any regularization for our reconstruction. To do so, the OUT is rotated; its orientation is changed into N different orientations $(\theta_i, i = 1, 2, \cdots, N)$; and the OUT is illuminated at each orientation. The electric fields are measured at v_{obs}; the radiating VECS's, the total internal electric fields, and the radiating contrast factors $\kappa_{r\,n}^{RAD}(\theta_i)$ of OUT at each orientation are estimated. Since the radiating contrast factor remains unchanged regardless of the incident angle, the *expected radiating contrast factor* is defined as follows:

$$\kappa_n^{Exp} = \frac{1}{N} \sum_{i=1}^{N} \mathcal{R}_{\theta_i}^{-1} \left\{ \kappa_{r\,n}^{RAD}(\theta_i) \right\}, \quad n = 1, 2, \cdots, q \quad (22)$$

The $\mathcal{R}_{\theta_i}^{-1}\{.\}$ operator rotates $\kappa_{r\,n}^{RAD}(\theta_i)$ for θ_i degrees to compensate for the rotation of the rotational stage.

To prevent solution instability, it is necessary to find the L_{RAD} threshold, which can be estimated using mean square error (MSE)[34, 35]. Using the MSE of the contrast factor, the L_{RAD} is obtained by minimizing the MSE of the approximated OUT boundary using the estimated radiating contrast factor,

$$L_{RAD} = \arg \min_{i=1}^{L_{noise}} \left\{ F(\kappa^{Exp\,i}) \right\}, \quad (23)$$

where F, is an OUT boundary-fit cost function.

The experimental results presented in the next section indicate that the location and the boundary of OUT can be successfully approximated by using the radiating permittivity profile and the radiating conductivity profile of ROI.

3 A Multi-view Near-field Scattering Tomography System

A multi-view NFST system is proposed in this section and shown as a block diagram in Figure 1. A horn antenna is used as the transmitting antenna and an open-ended waveguide is used as the receiving probe. The implemented NFST system is shown in Figure 2. To reduce system costs, the incident field remains unchanged at all times; instead, the OUT orientation is changed by utilizing a rotational stage as though OUT is illuminated from different angles. The NFST system is implemented and extensively evaluated by illuminating the OUT from different views (multi-view) without the need for fusing with the multi-frequency measurement results. A full rotation (360°) is employed to minimize shadowing effects in the multiple-view tomography system.

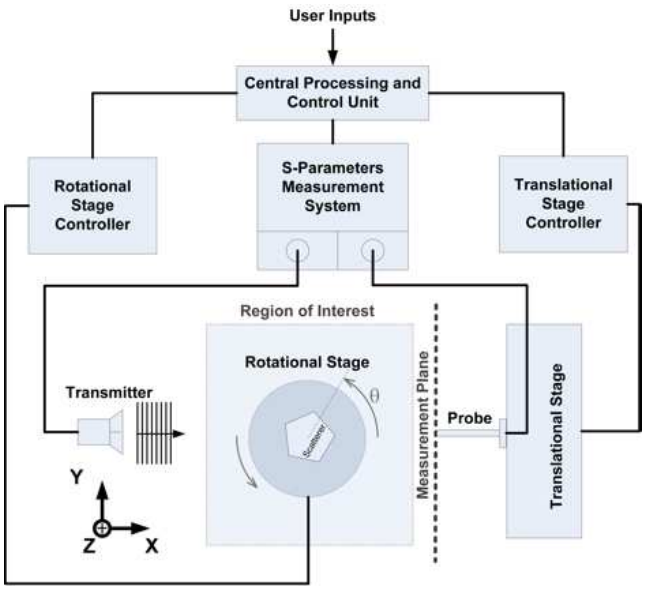

Fig. 1: The NFST system schematic.

The multipath effects can be efficiently controlled since most construction materials are very good absorbers of the electromagnetic fields at the millimeter-wave frequency range. Ceilings, floors, and walls absorb all the backscattered (indirect) signals. Therefore, the proposed system can be implemented in free space at the millimeter-wave and THz frequency range and does not need an Anechoic chamber or water as a background medium to control multipath effects. A thin absorber is used to control the multipath effects from a metallic surfaces. The proposed NFST system's advantages over the reported planar electromagnetic scattering systems are that it eliminates the need for 1) an Anechoic chamber or water as the background medium, 2) the translation stage for the transmitting antenna, and 3) the extra incident field measurements.

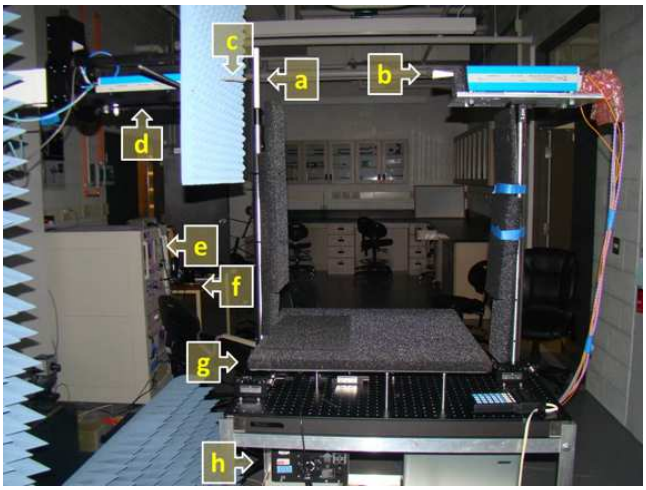

Fig. 2: The implemented multi-view NFST system picture with the components labeled as the (a) OUT, (b) transducer, (c) probe, (d) Y-Z translation stage, (e) PNA-X and Central processing and Control Unite, (f) Y-Z translation stage controller, (g) rotational stage, and (h) rotational stage controller.

In the implemented system, we have used a high precision scanner, the NSI-MI Near-field sub-millimeter scanner, with the spatial accuracy of 25 μm to conduct accurate measurements over the planar observation domain. The Keysight PNA-X Microwave Network Analyzer and OML millimeter-wave modules are used for s-parameters measurement. To facilitate system development at the frequency range, we built a new imaging setup that provides enough flexibility for aligning the source, scatterer, and observation planes accurately, as shown in Figure 2. The Thorlabs high resolution rotational stage with 1 *arcsec* accuracy is utilized to control the OUT orientation. An in-house developed code has been used to collect the measured data, estimate the radiating contrast factor, and reconstruct the scatterer's permittivity profile and the conductivity profile.

The multi-view NFST system implementation and operation involved the following steps:

Step 1)System calibration,
Step 2)Scanner initialization,
Step 3)The scattering parameter measurement and electric field calculation,
Step 4)Calculation the *radiating* contrast factor,
Step 5)Changes to the illumination angle, and repetition of the above measurements for different angles,
Step 6)Estimation of the *radiating* contrast factor, the permittivity profile and the conductivity profile,
Step 7)Determination of the L_{RAD} threshold once, first, for the calibration sample only.

The above seven steps are explained below. Step 1, system calibration, is very challenging and complex due to the small wavelength at the millimeter-wave frequency range. To facilitate system development at the frequency range, the detailed calibration procedures are as follows:

1. Initializing the system,
2. Discretizing of the region of interest (ROI) as shown in Figure 1,
3. Aligning the transmitting antenna's effective aperture, the receiving antenna's effective aperture, and the OUT lateral surface to achive the accuracy of half the maximum mesh size in the ROI or better (for the $2D$ case),
4. Localizing the rotation axis center and/or the OUT in the scan coordinate system (X, Y, Z) [36, 37],
5. Measuring the S_{21} over the ROI and the measurement domain,
6. Determining the S_{21}-to-E_{tot} conversion factor for free space and calibration OUT,
7. Estimating the incident electric field over the ROI and the measurement domain,

In Step 2, all of the measurement variables are initialized, and then, the scanner moves to the corresponding measurement location in the X, Y, and Z coordinates. In Step 3, the scattering parameters are measured using a network analyzer; then, the total electric field is calculated by using the S_{21}-to-E_{tot} conversion factor. In Step 4, the *radiating* contrast factor is estimated (19). In Step 5, the OUT is illuminated by the incident field at different angles until a full rotation is completed, and the expected radiating contrast factor is reconstructed by averaging the spatial radiating contrast factor estimated from multi-view measurements. In Step 6, the spatial radiating permittivity profile and the spatial conductivity profile are calculated from the averaged radiating contrast factor using (1). In Step 7, the L_{RAD} threshold is determinded for the calibration sample once by using (23).

4 Experimental results

In this section, we evaluate the effectiveness of the implemented multi-view planar NFST system by reconstructing the tomographic images of our samples by carrying out four independent experiments at the W-band (75 GHz − 110 GHz) frequency range. For this evaluation, we have used four isotropic and non-dispersive dielectric samples: two Teflon rods and two Teflon bars. The OUT is placed 16 mm away from the observation domain (measurement plane) for the multi-view near-field scattering tomography on the two objects: a Teflon rod with a 19.28 mm diameter, and a Teflon bar with 13 mm sides. Throughout these experiments, ROI is a 5 cm × 5 cm area on the $X - Y$ plane; the measurements are conducted along the Y-axis, and its span is set to 20 cm. The incident electric field polarization is considered to be linear and is aligned with the Z-axis. The Teflon bar and rod are shown in Figures 3 (a) and (b), respectively.

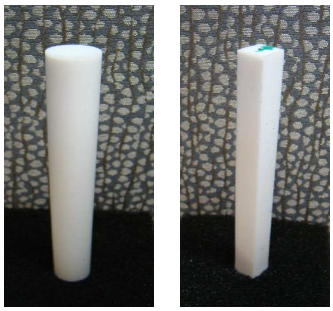

(a) (b)

Fig. 3: Teflon (a) rod and (b) bar.

In the first experiment, the rod with the 19.28 mm diameter is used as the calibration sample. To calibrate the system, the rod with its known dielectric constant and diameter, is illuminated with a plane wave, and the incident angle is varied in five-degree steps. L_{RAD} is determined. To maximize the expectation of detecting the OUT boundary, the L_{RAD} is obtained by minimizing the MSE of the contrast factor for the calibration rod sample object. Shown in Figure 4, the MSE curve indicates the first 17 singular values representing the radiating singular values. The scattered electric field and the VECS were projected into a new subspace spanned by the radiating singular scattered electric field and the radiating VECS orthonormal vectors (bases), respectively.

The rod reconstruction results are shown at a frequency of 75 GHz in Figure 5. The boundary of the object is shown by a dashed line. The sharp discontinuity, which enables us to distinguish OUT within ROI using the contrast factor and conductivity profile, does well represent the OUT boundary in Figures 5 (a), (b), and (d).

The above experimental measurement is repeated for a dielectric bar with the rectangular cross-section of sides 13 mm. The bar reconstruction results are shown in Figure 6. Some artifacts are noticeable in the reconstructed contrast factor of this bar due to

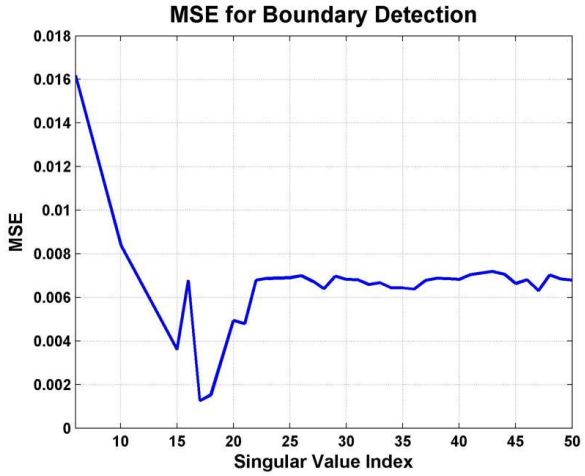

Fig. 4: The MSE of the expected radiating contrast factor versus the index of singular values.

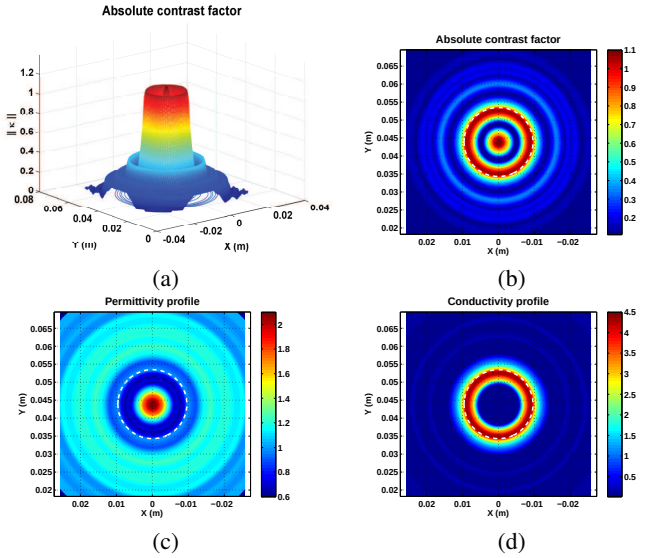

Fig. 5: The estimated radiating (a) contrast factor $3D$, (b) contrast factor, (c) permittivity profile, and (d) conductivity profile.

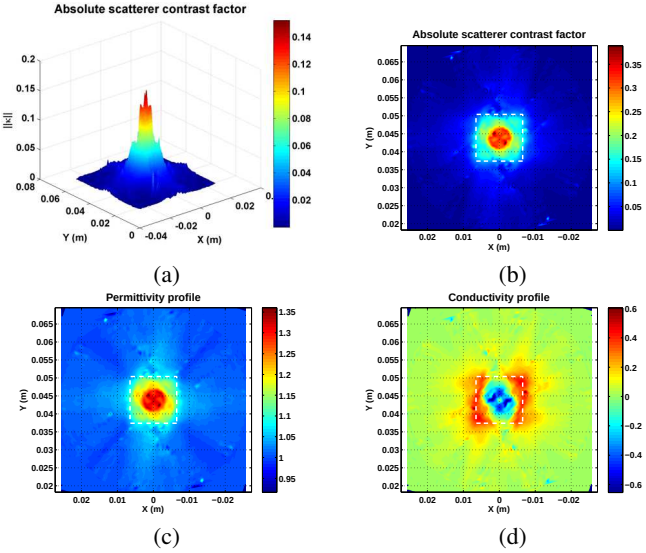

Fig. 6: The estimated radiating (a) contrast factor $3D$, (b) contrast factor, (c) permittivity profile, and (d) conductivity profile.

the roughness of the Teflon bar sides. The original sample boundary (dashed line) and the estimated one are in good agreement, as shown in Figures 6 (b) and (c). Since the Teflon loss tangent $(\frac{\sigma}{\omega\epsilon_0})$ is three order of magnitude smaller than its relative permittivity at the millimeter-wave frequency range, Equation (1) can be simplified to $\kappa_r = \epsilon_r - 1$. The Teflon permittivity profile dominates Equation (23), and the cost function can be considered almost insensitive to the conductivity. For that reason, the inconsistency between the estimated permittivity-and-conductivity ratio and the real permittivity-and-conductivity ratio are unavoidable and can be seen in Figures 5 and 6. Despite the inconsistency, the boundary of the OUT can be determined by utilizing the reconstructed estimated radiating contrast factor and conductivity profile as depicted in Figures 6 (b), and (d). Figures 5 (c) and 6 (c) show that the estimation errors of the expected permittivity profile are larger over the boundary of OUT. These errors could be prevented by considering the non-radiating permittivity profile [1] (which is not our focus in this paper).

For the next two experiments, the ROI mesh size is one-eighth of a wavelength, and the measurement span is subdivided into 241 segments at the frequencies of 75 GHz and 90 GHz. A 3.22 mm diameter Teflon rod and a bar with the 3.22 mm sides are used for the next two experiments.

In the third experiment, the Teflon rod with the 3.22 mm diameter is illuminated with the plane wave at the aforementioned frequencies. The distance between the measurement plane and the object is set to 33.4 mm for the far-field scattering tomography. The rod tomographic image reconstruction results are shown in Figure 7. The radiating permittivity profiles of the smaller size objects are smoother than those for the larger size objects since an object with a size smaller than a wavelength has less phase fluctuation than a larger object does. Additionally, as shown in Figures 7 (c) and (d), the permittivity profile error outside OUT at 90 GHz is less than at 75 GHz.

In the fourth experiment, the Teflon bar with the 3.22 mm sides is illuminated with the plane wave. The bar reconstruction results are shown in Figure 8. As we expected, the permittivity profile reconstructed at 90 GHz has higher resolution than the permittivity profile reconstructed at 75 GHz since we can see the edges and the corners at 90 GHz better than at 75 GHz. The reconstruction errors for the permittivity profile at 90 GHz are less than those at 75 GHz. The similarity between the contrast factor and the permittivity profile in Figures 7 and 8 at either 75 GHz or 90 GHz would be justified since Teflon is considered to be a lossless material at the millimeter-wave frequency range. By comparing Figures 6(b) and 8(c), we can acknowledge that the tomography system offers significantly better quality at the near-field region than the far field one. Owing to the higher number of radiating modes captured at the near-field region, the image quality is remarkably enhanced.

All of the above experiments verify that the implemented multi-view near-field scattering system successfully generates the tomographic image of an isotropic dielectric object with sufficient accuracy to determine the OUT boundary. Based on the reciprocity theory, the same results can be obtained if the OUT stays stationary, and the transmitter and receiving antenna orientation would change. Not only does the system allow operator to localize the OUT boundaries, but also potentially enables one to estimate the volumetric map of the electromagnetic properties of OUTs by utilizing the estimation technique reported in [1]. Furthermore, the tomography image resolution can be enhanced by adding the frequency-sweeping functionality to the near-field scattering tomography system for isotopic and non-dispersive dielectric objects.

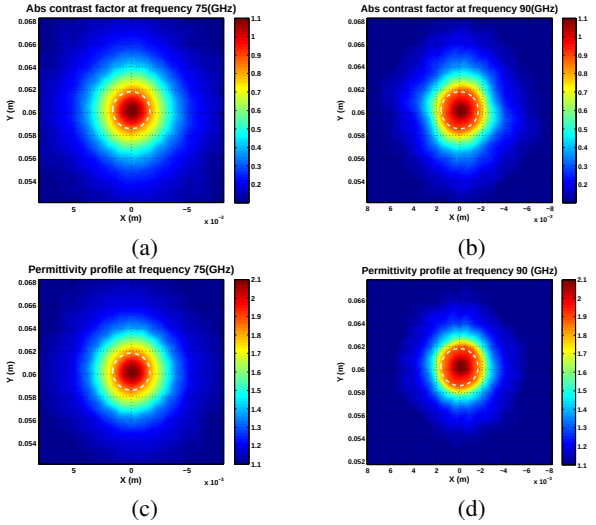

Fig. 7: Teflon rod far-field scattering tomography results: The estimated radiating parts of (a) contrast factor at 75 GHz, (b) contrast factor at 90 GHz, (c) permittivity profile at 75 GHz, and (d) permittivity profile at 90 GHz.

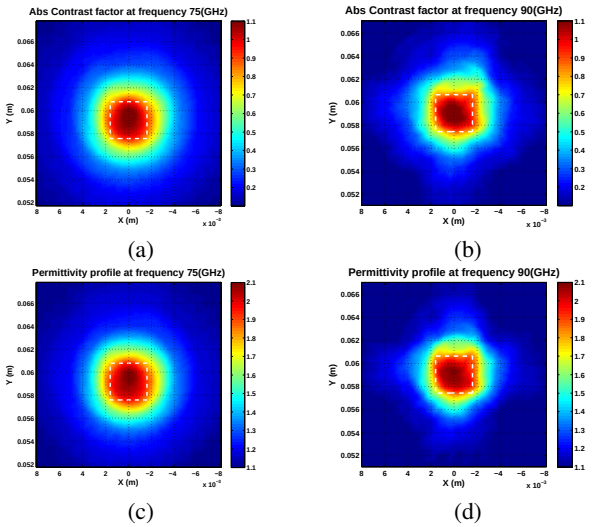

Fig. 8: Teflon bar far-field scattering tomography results: The estimated radiating parts of (a) contrast factor at 75 GHz, (b) contrast factor at 90 GHz, (c) permittivity profile at 75 GHz, and (d) permittivity profile at 90 GHz.

5 Conclusion

In this paper, a continuous-wave multi-view near-field scattering tomography (NFST) system is presented. The proposed system can be used to reconstruct the tomographic images and detect the boundary of an isotropic dielectric object. The signal subspace approach for solving the electromagnetic inverse scattering using continuous-wave is reformulated. The first non-linear imaging system is implemented and is evaluated successfully, and its calibration process is explained in detail. The advantages of the proposed system over other reported microwave scattering tomography systems are discussed. External multipath effects have been significantly reduced with the proposed system's configuration at the millimeter-wave frequency range, without the need for an Anechoic Chamber or water as a background medium. The proposed system can be considered the first stepping stone in developing non-linear imaging systems for clinical applications, pharmaceutical, and industrial applications (i.e. non-destructive test and quality assessment).

6 Acknowledgments

This work was supported by NSERC (Natural Sciences and Engineering Research Council) of Canada and BlackBerry (formerly Research In Motion).

The author would also like to thank Dr. Daniel J. van Rensburg of Nearfield System Inc. (NSI-MI), and Dr. Aidin Taeb of CIARS (Centre for Intelligent Antenna and Radio Systems) University of Waterloo for the valuable technical discussions and support and thank Ms. Mary McPherson for editing the paper manuscript.

7 References

1 Shahir, S., Mohajer, M., Rohani, A., et al., 'Permittivity Profile Estimation based on Non-radiating Equivalent Current Source (2D Case)', Progress In Electromagnetics Research B, 50 (1), 2013, pp. 157–175
2 Ermert, H., Dohlus, M., 'Microwave-diffraction-tomography of cylinderical objects using 3-Dimensionalwave-fields', NTZ Archiv : Archiv fur Nachrichtentechnik der ntz, 8 (1), 1986, pp. 110–117
3 Semenov, S.Y., Svenson, R.H., Boulyshev, A.E., et al., 'Microwave Tomography: Two-Dimensional System for Biological Imaging', Biomedical Engineering, , IEEE Transactions on, 43 (9), 1996, pp. 869–878
4 Herbert, F.L., 'Drawbacks and Limitations of Computed Tomography', Texas Hart Institute Journal, 31 (4), 2004, pp. 345–351
5 'What are the limitations of General Ultrasound Imaging?', Online, 2015, URL http://www.radiologyinfo.org/en/info.cfm?pg=genus
6 Larsen, L.E., Jacobi, J.H., 'Microwave interrogation of dielectric targets, Part I: By scattering parameters', Medical Physics, 5 (6), 1978, pp. 500–508
7 Larsen, L.E., Jacobi, J.H., 'Microwave scattering parameter imagery of an isolated canine kidney', Medical Physics, 6 (5), 1979, pp. 394–405
8 Jacobi, J.H., Larsen, L.E., Hast, C.T., 'Water-Immersed Microwave Antennas and Their Application to Microwave Interrogation of Biological Targets', Microwave Theory and Techniques, IEEE Transactions on, 27 (1), 1979, pp. 70–79
9 Ermert, H., Fülle, G., Hiller, D., 'Microwave Computerized Tomography', in 11th European Microwave Conference (1981), pp. 421–426
10 Bolomey, J., Izadnegandar, A., Jofre, L., et al., 'Microwave diffraction tomography for biomedical applications', Microwave Theory and Techniques, IEEE Transactions on, 30 (11), 1982, pp. 1998–2000
11 Pichot, C., Jofre, L., Peronnet, G., et al., 'Active Microwave Imaging of Inhomogeneous Bodies', Antennas And Propagation, IEEE Transactions on, 331 (4), 1985, pp. 416–428
12 Jofre, L., Hawley, M.S., Broquetas, A., et al., 'Medical imaging with a microwave tomographic scanner', Biomedical Engineering, IEEE Transactions on, 37 (3), 1990, pp. 303–312
13 Broquetas, A., Romeu, J., Rius, J.M., et al., 'Cylindrical geometry: A further step in active microwave tomography', Microwave Theory and Techniques, IEEE Transactions on, 39 (5), 1991, p. 836
14 Meaney, P.M., Paulsen, K.D., Hartov, A., et al., 'Near-Field Microwave Imaging of Biologically-Based Materials Using a Monopole Transceiver System', Microwave Theory and Techniques, IEEE Transactions on, 42 (1), 1995, pp. 1017–1027
15 Joachimowicz, N., Mallorqui, J.J., Bolomey, J., et al., 'Convergence and Stability Assessment of Newton-Kantorovich Reconstruction Algorithms for Microwave Tomography', Medical Imaging, IEEE Transactions on, 17 (4), 1998, pp. 562–570
16 Meaney, P.M., Paulsen, K.D., Chang, J.T., 'Near-Field Microwave Imaging of Biologically-Based Materials Using a Monopole Transceiver System', Microwave Theory and Techniques, IEEE Transactions on, 46 (1), 1998, pp. 31–46
17 Meaney, P.M., Fanning, M.W., Li, D., et al., 'A Clinical Prototype for Active Microwave Imaging of the Breast', Microwave Theory and Techniques, IEEE Transactions on, 48 (11), 2000, pp. 1841–1854
18 Fang, Q., Meaney, P.M., Paulsen, K.D., 'Singular value analysis of the Jacobian matrix in microwave image reconstruction', Antennas and Propagation, IEEE Transactions on, 54 (8), 2006, pp. 2371–2380
19 Amineh, R.K., Ravan, M., Khalatpour, A., et al., 'Three-Dimensional Near-Field Microwave Holography Using Reflected and Transmitted Signals', Antennas and Propagation, IEEE Transactions on, 59 (12), 2011, pp. 4777–4789
20 Mays, R.O., Behdad, N., Hagness, S.C., 'Array Sensitivity for Model-Based Microwave Breast Imaging', IEEE Transactions on Antennas and Propagation, 65 (6), 2017
21 Henriksson, T., Joachimowicz, N., Conessa, C., et al., 'Quantitative Microwave Imaging for Breast Cancer Detection Using a Planar 2.45 GHz System', Instrumentation and Measurment, IEEE Transactions on, 59 (10), 2010, pp. 2691–2699
22 Barton, N.P., 'Application of the optical transfer function to visual instruments', International Journal of Optics, 19 (6), 1972, pp. 473–484
23 Barton, N.P., 'The Use of Azimuth Scan MTF Technique for the Evaluation of Optical Components and Systems', in Assessment of Imaging Systems, (International Society for Optics and Photonics1976), pp. 82–89
24 Jacobi, J.H., Larsen, L.E., 'Microwave interrogation of dielectric targets, Part 2: By microwave time delay spectroscopy', Medical Physics, 5 (6), 1978, pp. 509–515
25 Peronnet, G., Pichot, C., Bolomey, J., et al., 'A Microwave Diffraction Tomography System for Biomedical Applications', in 1983 13th European Microwave Conference (1983), pp. 529–533
26 Bellomo, L., Pioch, S., Saillard, M., et al., 'Time Reversal Experiments In Microwave Range: Description of the Radar and Results', Progress In Electromagnetics Research, 104, 2010, pp. 427–448
27 Bellomo, L., Pioch, S., Saillard, M., et al., 'An Improved Antenna Calibration Methodology for Microwave Diffraction Tomography in Limited-Aspect Configurations', Antennas And Propagation, IEEE Transactions on, 62, 2014, pp. 2450–2463
28 Mehmet Abbak and Mehmet Çayören and İbrahim Akduman, 'Microwave breast phantom measurements with a cavity-backed Vivaldi antenna', IET Microwaves, Antennas & Propagation, 8, 2013, pp. 1127–1134
29 Picco, V., Negishi, T., Nishikata, S., et al., 'RF Tomography in Free Space: Experimental Validation of the Forward Model and an Inversion Algorithm Based on the Algebraic Reconstruction Technique', International Journal of Antennas and Propagation, Hindawi, 2013, 2013, pp. 1–10
30 Joachimowicz, N., Pichot, C., Hugonin, J.P., 'Inverse Scattering: An Iterative Numerical Method for Electromagnetic Imaging', Antennas and Propagation, IEEE Transactions on, 39 (19), 1991, pp. 1742–1752
31 Yu, C., Yuan, M., Stang, J., et al., 'Active Microwave Imaging II: 3-D System Prototype and Image Reconstruction From Experimental Data', Microwave Theory and Techniques, IEEE Trasnsaction on, 56 (4), 2008, pp. 991–1000
32 Slaney, M., Kak, A.C., Larsen, L.E., 'Limitations of imaging with first order diffraction tomography', Microwave Theory and Techniques, IEEE Transactions on, 32 (8), 1984, pp. 860–873
33 Harrington, R.F., Time-Harmonic Electromagnetic Fields, (The IEEE Press Series, Piscataway, NJ2001), 1st edition
34 Chew, W.C., Wang, Y.M., 'Reconstruction of Two-Dimensional Permittivity Distribution Using the Distorted Born Iterative Method', Medical Imaging, IEEE Transactions on, 9 (2), 1990, pp. 218–225
35 Chen, X., 'Application of Signal-subspace and optimization method in reconstructing extended scatterers', Journal of Optical Society of America, 26 (4), 2009, pp. 1022–1026
36 Ostadrahimi, M., AmerZakaria, LoVetri, J., et al., 'A Near-Field Dual Polarized (TE – TM) Microwave Imaging System', Microwave Theory and Techniques, IEEE Transactions on, 61 (3), 2013, p. 1376

37 Shahir, S., Orchard, J., Safavi-Naeini, S., 'Scatterer localization based on the non-radiating equivalent source', in Antennas and Propagation Society International Symposium (APSURSI), (IEEE2014), pp. 1924–1925